Shape-preserving chemical conversion of architected nanocomposites

Hendrikse, H.C.; Weijden, A. van der; Ronda-Lloret, M.; Yang, T.; Bliem, R.; Raveendran Shiju, N.; … ; Noorduin, W.L.

Shape-Preserving Chemical Conversion of Architected Nanocomposites

Hans C. Hendrikse, Arno van der Weijden, Maria Ronda-Lloret, Ting Yang, Roland Bliem, N. Raveendran Shiju, Martin van Hecke, Ling Li, and Willem L. Noorduin*

Forging customizable compounds into arbitrary shapes and structures has the potential to revolutionize functional materials, where independent control over shape and composition is essential. Current self-assembly strategies allow impressive levels of control over either shape or composition, but not both, as self-assembly inherently entangles shape and composition. Herein, independent control over shape and composition is achieved by chemical conversion reactions on nanocrystals, which are first self-assembled in nanocomposites with programmable microscopic shapes. The multiscale character of nanocomposites is crucial: nanocrystals (5–50 nm) offer enhanced chemical reactivity, while the composite layout accommodates volume changes of the nanocrystals (≈25%), which together leads to complete chemical conversion with full shape preservation. These reactions are surprisingly materials agnostic, allowing a large diversity of chemical pathways, and development of conversion pathways yielding a wide selection of shape-controlled transition metal chalcogenides (cadmium, manganese, iron, and nickel oxides and sulfides). Finally, the versatility and application potential of this strategy is demonstrated by assembling: 1) a scalable and highly reactive nickel catalyst for the dry reforming of butane, 2) an agile magnetic-controlled particle, and 3) an electron-beam-controlled reversible microactuator with sub-micrometer precision. Previously unimaginable customization of shape and composition is now achievable for assembling advanced functional components.

All around us, living organisms assemble 3D geometries with staggering complexity and sub-micrometer precision.[1–4] This has inspired synthetic assembly strategies to produce highly complex 3D shapes using simple methods.[4–18] Unfortunately, in both cases the choice of chemical compositions is limited. Alternatively, a wide selection of compositions can be reached by nanoparticle synthesis,[16,19–27] but assembling these in arbitrary

microscopic 3D shapes has remained challenging. Synthesis inherently entangles shape and composition; hence, current assembly routes offer control over either 3D shape or composition, but not both.

In principle, chemically converting existing 3D shapes to a specified composition allows control over both the chemical composition and 3D geometry. The viability of this strategy is indicated by naturally occurring geochemical fossilization processes,[1] and laboratory demonstrations of shape-preserving ion-exchange and oxidation/reduction reactions on individual and ensembles of nanocrystals, as well as biominerals.[5,23–28] Nevertheless, conversion of arbitrary microscopic architectures is still challenging as conversion is diffusion-limited and slow, and significant changes in the atomistic unit cells could yield uncontrollable dissolution/recrystallization, large deformations, and even fracture failure.

We recognize that successful conversion reactions require a paradoxical combination of reactivity and stability to enable: i) diffusion of reactants and products in the solid phase, ii) crystal lattice rearrangements and unit-cell volume changes, while iii) preserving the overall 3D shape. We thus hypothesize that nanocomposites consisting of nanocrystals in an amorphous matrix have excellent characteristics to overcome these issues. Traditionally, nanocomposites have mainly been studied for their excellent mechanical properties.[1,2,5,6,13,14] Importantly, coprecipitation of carbonate salts

H. C. Hendrikse, A. van der Weijden, Prof. M. van Hecke, Dr. W. L. Noorduin
AMOLF
Science Park 104, Amsterdam 1098 XG, The Netherlands
E-mail: noorduin@amolf.nl
M. Ronda-Lloret, Prof. N. R. Shiju
Van 't Hoff Institute for Molecular Sciences
University of Amsterdam
Science Park 904, Amsterdam 1090 GD, The Netherlands
T. Yang, Prof. L. Li
Department of Mechanical Engineering
Virginia Polytechnic Institute and State University
Blacksburg, VA 24060, USA

Dr. R. Bliem
ARCNL
Science Park 106, Amsterdam 1098 XG, The Netherlands
Dr. R. Bliem
Institute of Physics
University of Amsterdam
Science Park 904, Amsterdam 1098 XH, The Netherlands
Prof. M. van Hecke
Leiden Institute of Physics
Leiden University
Niels Bohrweg 2, Leiden 2333 CA, The Netherlands

The ORCID identification number(s) for the author(s) of this article can be found under https://doi.org/10.1002/adma.202003999.

DOI: 10.1002/adma.202003999

and silica enables the formation of nanocomposites that can be sculpted into a wide diversity of shapes ranging from stems and coral-like forms to helices by modulating the reaction conditions such as temperature, pH, and CO_2 concentration.[8–10,29–31] However, the reaction mechanism restricts the chemical composition of the resulting nanocomposites to amorphous silica and crystalline barium, strontium, or calcium carbonate. Consequently, the resulting nanocomposites have limited functionalities by themselves. However, we note that many interesting metal compounds form carbonate salts with closely related crystal structures. These similarities may facilitate ion exchange with minimal rearrangements of the crystal lattice toward a wide range of metal chalcogenides with interesting chemical and electronic properties.

Here we show that the unique structuring across length scales of nanocomposites enables a versatile and surprisingly amenable shape-preserving conversion strategy, thus enabling a complete uncoupling of the 3D shape from the chemical composition. We first investigate the general processes for shape-preserving conversion reactions by studying a representative case: the conversion of barium carbonate ($BaCO_3$) to cadmium sulfide (CdS) in coral-shaped $BaCO_3/SiO_2$ nanocomposites. The initial $BaCO_3/SiO_2$ coral-like shapes are synthesized following these previously developed procedures (see Section S1, Supporting Information, for details).[9] Our conversion scheme consists of a two-step pathway, that is motivated by the solubilities, chemical reactivities, and crystallographic similarities of orthorhombic $BaCO_3$, the intermediate trigonal $CdCO_3$, and trigonal CdS.[28,32]

First, $BaCO_3$ is converted to $CdCO_3$ by immersing the shapes into an aqueous solution of $CdCl_2$ (50 mM) at room temperature for 10 min (**Figure 1**; see Section S2, Supporting
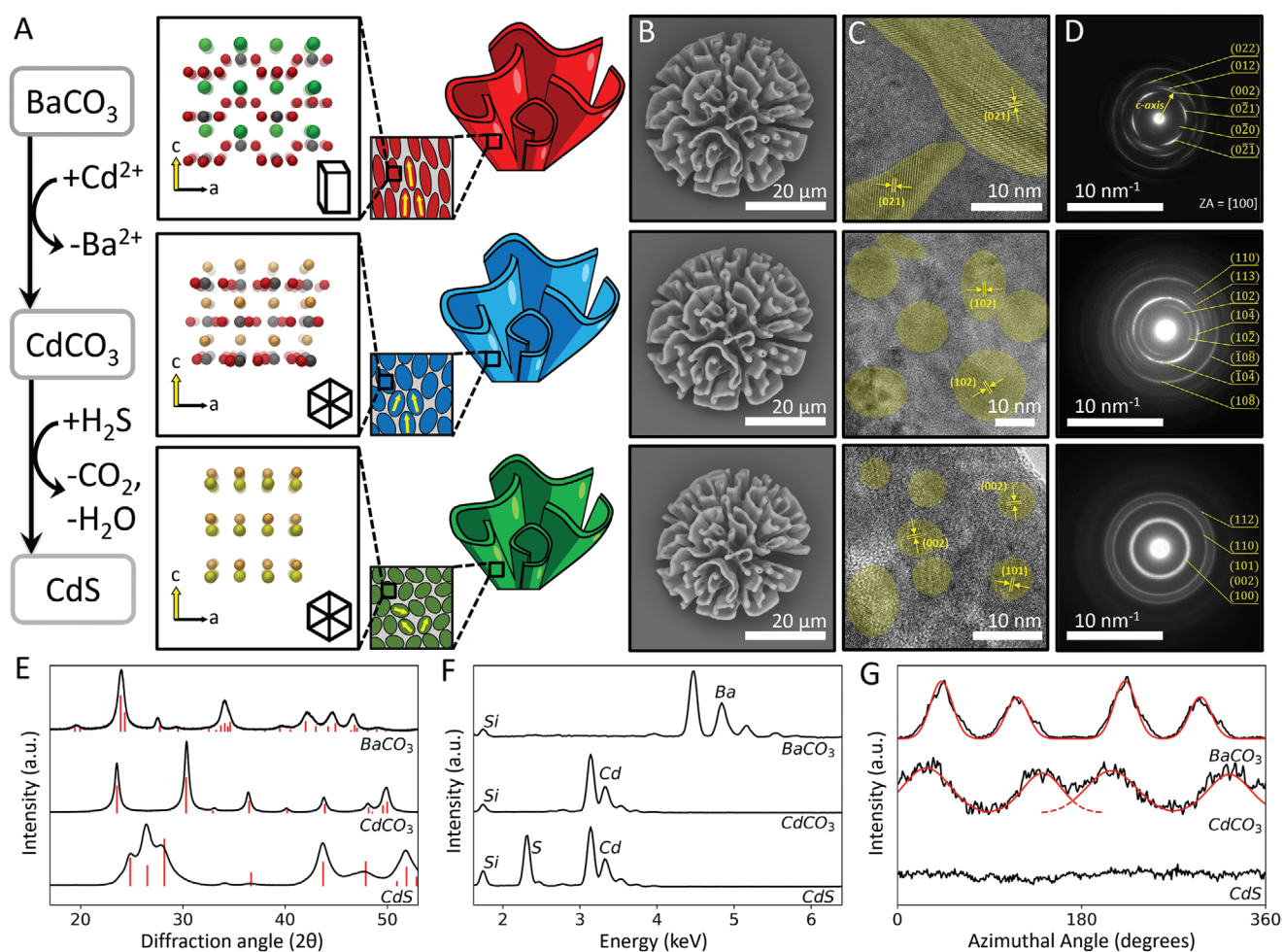

Figure 1. Shape-preserving conversion in nanocomposites. A) Reaction steps, crystal structures, and schematic hierarchical organization of the nanocomposites. B) SEM backscatter images of the same architecture showing shape preservation and volume adjustment after each reaction step. C) TEM imaging of FIB-sectioned architectures show preservation of crystallinity and nanocomposite layout after each reaction step, nanocrystallites highlighted in color (see Section S10, Supporting Information, for details). D) SAED on cross-sections show preservation of crystallinity, crystallographic orientation of the *c*-axis indicted by the yellow arrow (TEM was performed on different architectures than shown in (B); see Section S10, Supporting Information, for details). E) XRD, and F) EDS confirm complete chemical conversion (red lines indicate XRD spectra of the expected products). XRD peak positions are consistent with the observed nanocrystal sizes in (C). G) Demonstration of crystallographic misorientations by integrating selected diffraction peaks with respect to the azimuthal angle from the SAED data in (D). The diffraction peaks used for analysis are $(0\bar{2}1)/(0\bar{2}\bar{1})/(02\bar{1})/(021)$, $(10\bar{2})/(102)/(\bar{1}02)/(\bar{1}0\bar{2})$, and $(101)/(002)/(100)$ peaks for $BaCO_3$, $CdCO_3$, and CdS, respectively. The black and red lines represent the experimental and fitting results.

**ADVANCED
SCIENCE NEWS**
www.advancedsciencenews.com

**ADVANCED
MATERIALS**
www.advmat.de

Information, for details). This cation exchange is driven toward the formation of $CdCO_3$ by the 1000-fold lower solubility of $CdCO_3$ ($K_{sp,CdCO_3} = 1.0 \times 10^{-12}$) compared to $BaCO_3$ ($K_{sp,BaCO_3} = 2.58 \times 10^{-9}$), and the excess amount of Cd^{2+} in the solution. Second, $CdCO_3$ is converted to CdS in H_2S/N_2 10/90 vol% at 1 bar and 290 °C for 4 h. This anion exchange is facilitated by the release of H_2O and CO_2. Scanning electron microscopy (SEM) shows excellent preservation of the 3D microscopic shape (Figure 1B), while X-ray powder diffraction (XRD) and energy dispersion spectroscopy (EDS) analysis confirm the complete chemical conversion to yield trigonal $CdCO_3$ in step 1, and trigonal CdS in step 2 (Figure 1E,F).

To disentangle the mechanism underlying microscopic shape preservation during (volume) changes of the crystallographic unit cells, we compare architectures before and after each exchange step at various length scales. During the intermediate conversion of $BaCO_3$ to $CdCO_3$ the volume of the crystal lattice shrinks by ≈25%. However, comparison of the microscopic shape before and after the conversion to $CdCO_3$ shows no volume change, suggesting the formation of nanopores in the composite (Figure 1; Section S11, Supporting Information). During the final conversion from $CdCO_3$ to CdS, the volume of the crystal lattice shrinks an additional 11%, and the volume of the microscopic shape shrinks almost 30%, implying the disappearance of the nanoporosity. Indeed, the volume change of the overall conversion of $BaCO_3$ to CdS (33%) is almost identical for the crystal structure volume and microscopic shape (30%, see Section S11, Supporting Information): volume changes of the crystal lattice are thus translated to mesoscale volume changes of the architecture.

Remarkably, albeit shrunken, the final CdS microshape is geometrically indistinguishable from the original one; even sub-micrometer details remain preserved. We follow the conversion processes at the nanoscale using transmission electron microscopy (TEM) imaging and selected-area electron diffraction (SAED). In the original $BaCO_3/SiO_2$ nanocomposites, the $BaCO_3$ nanocrystals exhibit rod-like morphologies (length, ≈20–50 nm; width, ≈5–10 nm) (Figure 1C),[8,10] which are preferentially oriented with the *c*-axis along the growth direction of the nanocomposite (Figure 1D; Figure S20, Supporting Information). The azimuthally integrated intensity profile of selected diffraction peaks allows us to estimate the crystallographic misorientation distribution of ≈25° within the silica matrix (Figure 1D,G; see Section S10, Supporting Information). Facilitated by the similarities between the crystal structures, this preferred co-alignment along the *c*-axis is maintained after the conversion to trigonal $CdCO_3$, although the misorientation distribution increases to ≈50° (Figure 1D). In addition, the $CdCO_3$ crystals slightly shrink to ≈20 nm and appear to lose their rod-like morphologies. During the more profound rearrangement of the crystal structure into trigonal CdS the nanocrystals shrink further to 5–10 nm and become randomly oriented (Figure 1D). Throughout these transformations, the hydrated silica matrix is preserved and the nanocrystals remain embedded in the matrix (Figure 1C). The combined effects from the composite nature, nanoscopic structural features, and hydrated silica,[33] thus allow the structure to maintain its 3D shape without significant fracture problems. We conclude that the matrix adapts to the shape transformations

and reorientations at the nanoscale while preserving the overall shape at the microscale.

Complete chemical conversion requires rapid transport of ions toward and away from the nanocrystals through the entire architecture. We envisage that the interconnected silica matrix, which constitutes ≈15–20 at% of the overall composite, can facilitate this transport. Consistent with this hypothesis, deliberately crosslinking the silica matrix by heating hinders the diffusion of ions and thereby leads to incomplete conversion. In addition, removing the silica matrix results in poor conversion or even destruction of the architectures, thus emphasizing the role of the percolating matrix for both transport and stabilization of the overall shape.

Overall, the multiscale character of nanocomposites is perfectly suited for the essential processes of/during shape-preserving conversion reactions. The large surface to volume ratio of the nanocrystals enhances chemical reactivity, the percolating silica matrix enables transport of ions, and the composite layout provides mechanical stability for preserving the overall morphology during expansion and shrinkage of the crystal unit cell.

These insights suggest that once a suitable chemical pathway is established, shape-preserving conversion can be achieved for a wide palette of chemical compositions and shapes by taking advantage of the nanocomposite layout. To demonstrate this, we design a general conversion pathway toward metal chalcogenides which are of wide interest for their chemical and electronic properties,[34] and where control over their form offers improved or even novel applications. Our strategy is motivated by the following considerations: i) many relevant transition metals form carbonates,[32] which facilitates cation exchange, ii) many metal carbonates crystallize in the same or related crystal structures, which facilitates cation exchange with a minimal distortion of the anionic framework, iii) the carbonate anion can act as a good leaving group for introducing the desired oxide or sulfide, and iv) the oxidation state of the metal can be controlled by applying either oxidative or reductive conditions.

To demonstrate that our process is essentially independent of the shape of the nanocomposite and the details of the chemical pathway, we converted $BaCO_3/SiO_2$ nanocomposites (e.g., coral-, spiral-, vase-, and post-like shapes) into a range of cadmium-, iron-, manganese-, and nickel-oxides and sulfides (see Sections S2–S8, Supporting Information, for details). SEM analysis, EDS mapping, and XRD confirm the chemical conversion with preservation of the microscopic geometry and nanocomposite layout (**Figure 2**). We find that the nanocomposite layout also supports the formation of amorphous phases (e.g., nickel and iron carbonate) and a wide range of crystal structures (e.g., orthorhombic, cubic, tetragonal, trigonal). In addition, the oxidation state of the metals can be controlled. Inspired by previous studies,[35–37] we heat nanocomposites of iron carbonate to yield shape-controlled architectures of magnetite $Fe(II,III)_3O_4$ under inert conditions, hematite α-$Fe(III)_2O_3$ under oxidative conditions with O_2, and even metallic iron δ-Fe under reductive conditions with H_2. Our design strategy thus offers a systematic, versatile, and highly customizable route toward a wide range of chemical compositions with independent control over the microscopic architecture.
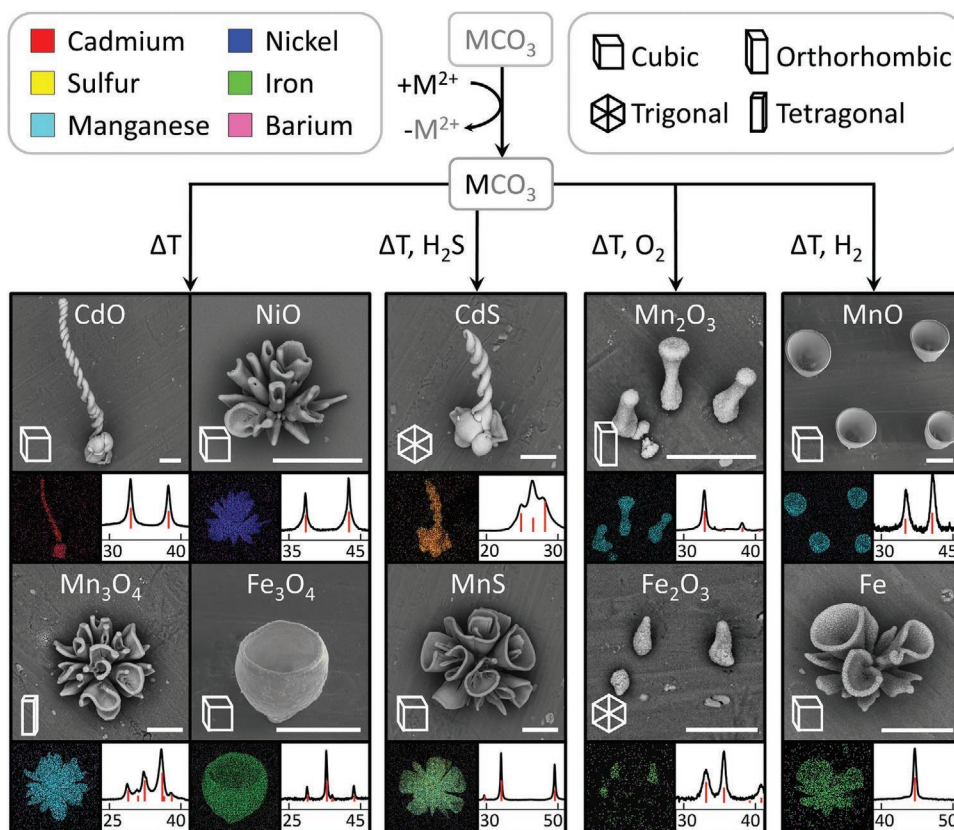
Figure 2. Conversion pathways to metal oxides and metal sulfides. SEM micrographs show the shape preservation (scale bars 10 µm), while EDS mapping and XRD confirm the conversion (EDS colormap according to top left panel; XRD reference peaks indicated in red, final crystal system indicated by icon). First the desired metal ion is introduced; subsequently the desired metal chalcogenide is obtained by heating the architecture in a chemical vapor deposition reactor (see Sections S2–S6, Supporting Information, for details).

We demonstrate the versatility and application potential of our approach by designing three different examples of functional self-assembled components, relevant for catalysis, magnetic movement, and electron-beam-induced actuation. First, for many supported metal oxide catalysts, it is desirable to have architectures with high specific surface areas that are easily accessible, with short distances between the catalyst and support surfaces, and 10–20 nm sized nanocrystals.[38,39] From this perspective, metal oxide/SiO_2 coral-like shapes are ideal as they provide a large reactive surface that is easily accessible for the reagents and products while the nanocomposite layout offers extremely short distances between the two surfaces that take part in the reaction. We explore this potential by developing Ni/SiO_2 coral-like shapes (Ni_{coral}) for the dry reforming reaction, where C_4H_{10} and CO_2 are converted to syngas (H_2 and CO) (**Figure 3**A). Due to the high thermodynamic stability of CO_2 and chemical inertness of C−H bonds in lower alkanes, this reaction normally requires high temperatures (>600 °C).[40,41] To develop more sustainable catalysts, lowering the reaction temperature is essential but remains challenging.[42] At a desirable low temperature for this reaction (400 °C),[42] conventionally prepared catalysts ($Ni_{convent}$, ≈5/95 at% Ni/Si, ≈21 nm Ni crystals) shows no detectable activity, which can be attributed to their lower metal loading. Alternatively, a conventional catalyst with a high metal loading equivalent to Ni_{coral}

mainly shows undesired byproducts (Ni_{equiv}, ≈80/20 at% Ni/Si, ≈105 nm Ni crystals). Excitingly, our nanocomposite Ni catalysts (≈80/20 at% Ni/Si, ≈21 nm Ni crystals; see Sections S9 and S12, Supporting Information, for details) are active at 400 °C and predominantly form the desired CO and H_2 products (Figure 3B,C; see Section S13, Supporting Information, for details). These results demonstrate a unique strength of our approach; the direct integration of nanocrystals and SiO_2 support enables high metal concentrations for high catalytic reactivity and nanosized crystals for improved catalytic selectivity. Importantly, we leverage bottom-up assembly to make large quantities of material: while a single component only weighs tens of nanograms, we demonstrate the catalytic activity on the gram scale.

Second, the nanocomposite layout enables the translation of unique nanoscale properties to microscopic behavior. We demonstrate this potential by developing corals that are composed of iron oxide (Fe_3O_4) nanocrystals (Figure 3D). Fe_3O_4 is magnetic, suggesting that these nanocrystals can be controllably moved by external magnetic fields.[15,22] Indeed, we find that the quasi-spherical circumference of coral-like forms in combination with the magnetic nanocomposite interior enables agile control using an external magnet to achieve rotation along all axes for orientation and rolling, as well as lateral movement with great fidelity (Figure 3D,E). In addition, these magnetically
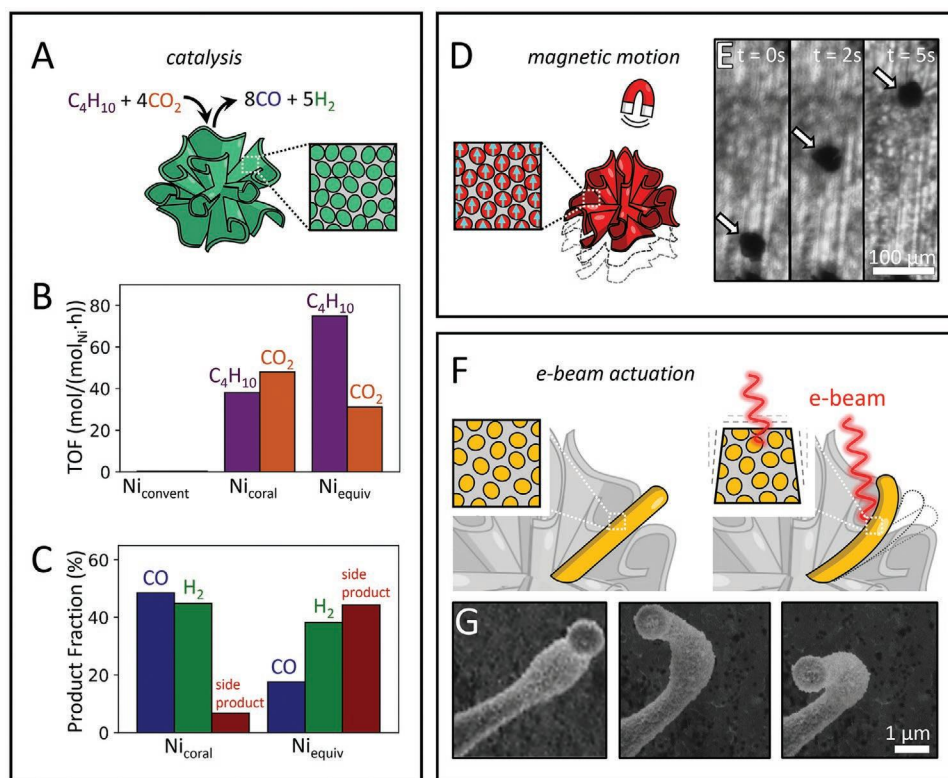
Figure 3. Functional shape/composition-controlled nanocomposites. A) Catalyzed dry reforming of butane on Ni_{coral}. B) Catalytic turnover frequency (TOF) for C_4H_{10} (purple) and CO_2 (orange) at 400 °C, showing no activity for 5 wt% conventional catalysts $Ni_{convent}$, and comparable activity for nanocomposite catalysts Ni_{coral} and catalysts with equivalent metal loading Ni_{equiv}. C) Product fraction for CO (blue), H_2 (green), and side products (methane, ethane, ethylene, and solid carbon depositions (coke)) (red), showing good selectivity for Ni_{coral}, and predominantly side product formation for Ni_{equiv}. (see Section S13, Supporting Information, for details). D) Magnetic-controlled locomotion, with E) optical microscopy time-lapse series of coral-like nanocomposite of magnetic Fe_3O_4 nanocrystals. (see Section S14, Supporting Information, for details). F) Electron-beam-induced actuation of nanocomposites with low nanocrystal loading (60–70% metal) that provides directional shielding of the shrinking silica matrix and mechanical flexibility for deformation. G) SEM series showing e-beam-controlled actuation on selected area, 5 kV, 2.1 pA μm^{-2} (see Movies S1–S3 and Section S15, Supporting Information, for details).

controlled locomotive particles can transport cargo such as microfibers (see Section S14, Supporting Information).

Finally, the mechanical flexibility of our nanocomposites not only accommodates volume changes during conversion reactions, but can also be exploited for actuation with sub-micrometer precision. It is well known that silica can undergo shrinking during electron-beam irradiation.[43] We exploit this effect to achieve highly controllable actuation: partially removing the nanocrystals (≈60–70 at%) limits the penetration depth of the e-beam in the composite while maintaining sufficient mechanical flexibility. Consequently, one side of the silica matrix can be exposed to the e-beam and shrinks, while the other side is shielded by the nanocrystals and remains unaffected, thus leading to extremely large bending deformations toward the e-beam (Figure 3F,G). Exposing preassigned areas of the composite to e-beam irradiation results in directed actuation, even over different parts within a single architecture, while alternating irradiating either side of the composite enables oscillating movements (see Section S15 and Movies S1–S3, Supporting Information).

In summary, we introduce a versatile strategy for shape-controlled architectures with tailored functionalities. The design principles are highly customizable owing to the broad choice of chemistries, and leverage scalability and practical simplicity of directed assembly strategies. We foresee that the multiple complementary functionalities can be integrated by exploiting orthogonal chemistry approaches for tuning the chemical composition of the nanocrystals, and functionalizing or replacing the amorphous silica matrix with well-developed chemistries.[29,44,45] Combining coprecipitation reactions with top-down fabrication strategies may enable the sculpting of nanocomposite resins according to exact designs that subsequently can be converted into arbitrary chemical compositions. Moreover, these conversion reactions may be applied to bestow other synthetic and biological nanocomposites with unusual and attractive combinations of properties, ultimately enabling applications ranging from potent catalysts and actuatable sensors to high-performance batteries and magneto-optical materials.

Experimental Section

For details, see Sections S1–S6, Supporting Information.

Synthesis of $BaCO_3/SiO_2$ Nanocomposites: $BaCO_3/SiO_2$ nanocomposites were synthesized according to previously published methods (see Section S1, Supporting Information).[9]

General Synthesis of MCO₃ (M = Mn, Fe, Ni, Cd) Nanocomposites: MNO₃ or MCl₂ (2.5–5 mmol) was dissolved in 50 mL degassed water. Subsequently a substrate with freshly converted BaCO₃/SiO₂ nanocomposites was placed in this solution for 10–80 min. The resulting MCO₃ microarchitectures were washed in two demineralized water baths followed by an acetone bath. After drying in the air, the structures were analyzed using SEM, XRD, and EDS (see Sections S2–S8, Supporting Information).

General Conversion to MO$_x$ or MS Nanocomposites: A substrate containing MCO₃ nanocomposites was placed in a single zone tube furnace and heated to 290–900 °C in a N₂ or Ar atmosphere at 1 bar. The furnace was kept at a stable temperate for a time between 10 min and 24 h. Upon reaching stable temperature, H₂S (10 vol%), H₂ (5 vol%), or O₂ (20 vol%) could be added to the gas flow to control the anion and oxidation state of the resulting nanocomposite. After this the tube furnace was flushed with pure N₂ or Ar gas and allowed to cool. The resulting MO$_x$ or MS microarchitectures were characterized by XRD, SEM, and EDS (see Sections S2–S8, Supporting Information).

Supporting Information

Supporting Information is available from the Wiley Online Library or from the author.

Conflict of Interest

The authors declare no conflict of interest.

[1] M. Eder, S. Amini, P. Fratzl, *Science* **2018**, *362*, 543.

[2] R. Weinkamer, P. Fratzl, *MRS Bull.* **2016**, *41*, 667.

[3] F. C. Meldrum, H. Cölfen, *Chem. Rev.* **2008**, *108*, 4332.

[4] H. A. Lowenstam, S. Weiner, *On Biomineralization*, Oxford University Press, New York **1989**.

[5] M. R. Begley, D. S. Gianola, T. R. Ray, *Science* **2019**, *364*, eaav4299.

[6] F. L. Bargardi, H. Le Ferrand, R. Libanori, A. R. Studart, *Nat. Commun.* **2016**, *7*, 13912.

[7] P. Knoll, O. Steinbock, *Isr. J. Chem.* **2018**, *58*, 682.

[8] J. M. Garcia-Ruiz, E. Melero-Garcia, S. T. Hyde, *Science* **2009**, *323*, 362.

[9] W. L. Noorduin, A. Grinthal, L. Mahadevan, J. Aizenberg, *Science* **2013**, *340*, 832.

[10] C. N. Kaplan, W. L. Noorduin, L. Li, R. Sadza, L. Folkertsma, J. Aizenberg, L. Mahadevan, *Science* **2017**, *355*, 1395.

[11] G. M. Whitesides, *Science* **2002**, *295*, 2418.

[12] Z. Bao, M. R. Weatherspoon, S. Shian, Y. Cai, P. D. Graham, S. M. Allan, G. Ahmad, M. B. Dickerson, B. C. Church, Z. Kang, H. W. Abernathy III, C. J. Summers, M. Liu, K. H. Sandhage, *Nature* **2007**, *446*, 172.

[13] A. R. Studart, *Adv. Mater.* **2012**, *24*, 5024.

[14] U. G. K. Wegst, H. Bai, E. Saiz, A. P. Tomsia, R. O. Ritchie, *Nat. Mater.* **2015**, *14*, 23.

[15] G. Mirabello, J. J. M. Lenders, N. A. J. M. Sommerdijk, *Chem. Soc. Rev.* **2016**, *45*, 5085.

[16] N. Vogel, M. Retsch, C.-A. Fustin, A. Del Campo, U. Jonas, *Chem. Rev.* **2015**, *115*, 6265.

[17] X. Xia, A. Afshar, H. Yang, C. M. Portela, D. M. Kochmann, C. V. Di Leo, J. R. Greer, *Nature* **2019**, *573*, 205.

[18] W. J. Choi, G. Cheng, Z. Huang, S. Zhang, T. B. Norris, N. A. Kotov, *Nat. Mater.* **2019**, *18*, 820.

[19] E. V. Shevchenko, D. V. Talapin, N. A. Kotov, S. O'brien, C. B. Murray, *Nature* **2006**, *439*, 55.

[20] P. K. Kundu, D. Samanta, R. Leizrowice, B. Margulis, H. Zhao, M. Börner, T. Udayabhaskararao, D. Manna, R. Klajn, *Nat. Chem.* **2015**, *7*, 646.

[21] J.-H. Choi, H. Wang, S. J. Oh, T. Paik, P. Sung, J. Sung, X. Ye, T. Zhao, B. T. Diroll, C. B. Murray, C. R. Kagan, *Science* **2016**, *352*, 205.

[22] G. Singh, H. Chan, A. Baskin, E. Gelman, N. Repnin, P. Kral, R. Klajn, *Science* **2014**, *345*, 1149.

[23] B. J. Beberwyck, Y. Surendranath, A. P. Alivisatos, *J. Phys. Chem. C* **2013**, *117*, 19759.

[24] M. P. Boneschanscher, W. H. Evers, J. J. Geuchies, T. Altantzis, B. Goris, F. T. Rabouw, S. A. P. Van Rossum, H. S. J. Van Der Zant, L. D. A. Siebbeles, G. Van Tendeloo, I. Swart, J. Hilhorst, A. V. Petukhov, S. Bals, D. Vanmaekelbergh, *Science* **2014**, *344*, 1377.

[25] A. Putnis, *Science* **2014**, *343*, 1441.

[26] A. E. Powell, J. M. Hodges, R. E. Schaak, *J. Am. Chem. Soc.* **2016**, *138*, 471.

[27] K. J. Stebe, E. Lewandowski, M. Ghosh, *Science* **2009**, *325*, 159.

[28] T. Holtus, L. Helmbrecht, H. C. Hendrikse, I. Baglai, S. Meuret, G. W. P. Adhyaksa, E. C. Garnett, W. L. Noorduin, *Nat. Chem.* **2018**, *10*, 740.

[29] J. Opel, F. P. Wimmer, M. Kellermeier, H. Cölfen, *Nanoscale Horiz.* **2016**, *1*, 144.

[30] L. Helmbrecht, M. Tan, R. Röhrich, M. H. Bistervels, B. O. Kessels, A. F. Koenderink, B. Kahr, W. L. Noorduin, *Adv. Funct. Mater.* **2020**, *30*, 1908218.

[31] G. Zhang, C. Verdugo-Escamilla, D. Choquesillo-Lazarte, J. M. García-Ruiz, *Nat. Commun.* **2018**, *9*, 5221.

[32] K. H. Stern, *High Temperature Properties and Thermal Composition of Inorganic Salts*, CRC Press, Boca Raton, FL, USA **2001**.

[33] K. R. Phillips, N. Vogel, Y. Hu, M. Kolle, C. C. Perry, J. Aizenberg, *Chem. Mater.* **2014**, *26*, 1622.

[34] M.-R. Gao, Y.-F. Xu, J. Jiang, S.-H. Yu, *Chem. Soc. Rev.* **2013**, *42*, 2986.

[35] A. M. Hirt, *Iron Oxides: From Nature to Applications*, Wiley-VCH, Weinheim, Germany **2016**.

[36] H. E. Kissinger, H. F. Mcmurdie, B. S. Simpson, *J. Am. Ceram. Soc.* **1956**, *39*, 168.

[37] A. Navrotsky, C. Ma, K. Lilova, N. Birkner, *Science* **2010**, *330*, 199.

[38] P. Munnik, P. E. De Jongh, K. P. De Jong, *Chem. Rev.* **2015**, *115*, 6687.

[39] P. Lanzafame, S. Perathoner, G. Centi, S. Gross, E. J. M. Hensen, *Catal. Sci. Technol.* **2017**, *7*, 5182.

[40] B. Yan, X. Yang, S. Yao, J. Wan, M. Myint, E. Gomez, Z. Xie, S. Kattel, W. Xu, J. G. Chen, *ACS Catal.* **2016**, *6*, 7283.

[41] R. Singh, A. Dhir, S. K. Mohapatra, S. K. Mahla, *Biomass Convers. Biorefin.* **2020**, *10*, 567.

[42] Y. Wang, L. Yao, S. Wang, D. Mao, C. Hu, *Fuel Process. Technol.* **2018**, *169*, 199.

[43] R. A. Sigsbee, R. H. Wilson, *Appl. Phys. Lett.* **1973**, *23*, 541.

[44] C. J. Brinker, G. W. Scherer, *Sol-Gel Science*, Academic Press, London, UK **1990**.

[45] J. Opel, J. Brunner, R. Zimmermanns, T. Steegmans, E. Sturm, M. Kellermeier, H. Cölfen, J.-M. García-Ruiz, *Adv. Funct. Mater.* **2019**, *29*, 1902047.